Proceedings of the 7th International Symposium on Cavitation
CAV2009 – Paper No. 53
August 17-22, 2009, Ann Arbor, Michigan, USA

Influence of shock-bubble and bubble-bubble interactions on the collapse of a cluster of bubbles

Kazumichi Kobayashi
Osaka Prefecture University
Sakai, Osaka, Japan

Yoshinori Jinbo
Osaka Prefecture University
Sakai, Osaka, Japan

Hiroyuki Takahira
Osaka Prefecture University
Sakai, Osaka, Japan

ABSTRACT

The present work is concerned with direct numerical simulations for the shock-bubble and bubble-bubble interactions using the improved ghost fluid method in which the Riemann solutions are utilized to diminish numerical oscillations near interfaces. The influence of bubble size and bubble-bubble distance on the collapse of in-line two bubbles and in-line three bubbles are investigated to understand the conditions under which the bubble-bubble interactions accelerate or decelerate the bubble collapse. It is shown that when the in-line bubbles collapse by the incident shock wave, the collapse of the downstream bubble can be accelerated by the shock waves due to the collapse of upstream bubbles, while the collapse of the upstream bubbles is decelerated by the expansion wave cased by the reflection of the incident shock wave at the surface of the downstream bubbles. Also, there exists the bubble-bubble distance in which the collapse of the downstream bubble is most accelerated. When the downstream bubble is smaller than the upstream bubble, the downstream bubble collapses more violently than the single bubble at any distance between the bubbles. The phase of the downstream bubble at the impact of the shock waves generated from the upstream bubbles is important in determining the acceleration of the collapse of the downstream bubble. It is also shown that the pressure increase in liquid near the axis of symmetry around the downstream bubble increases with the increase of number of bubbles and with the decrease of the bubble-bubble distance because the pressure increase in liquid is caused by the superposition of the shock waves generated from all bubbles.

INTRODUCTION

Mutual interactions among bubbles in a liquid are a fundamental problem of cavitation, which must be clarified to understand phenomena such as material damage, noise, and performance drop of hydraulic machinery [1]. Recently, the phenomena related to bubble collapse are extended to various fields. For example, the material damage due to cavitation bubble collapse in the liquid-mercury target systems for high-intense pulsed-spallation neutron sources is a big problem to be overcome in order to make a lifetime of the systems longer; the cavitation bubbles are generated by the negative pressure that is caused by the pressure waves generated in the mercury due to rapidly deposited heat energy from the proton beams that interact with the vessel wall. To reduce the cavitation inception, the injection of gas bubbles into liquid-mercury has been conducted, which reduces the pitting damage due to the bubble collapse [2, 3].

In the medical applications, Extracorporeal Shock Wave Lithotripter (ESWL) has been widely used for urinary lithiasis. In ESWL, the shock waves generated outside of human body are utilized to crush the calculi in patients' body. When the calculi are crushed, however, cavitation bubbles are formed near the calculi. The cavitation bubbles cause tissue damages [4]. The acoustic cavitation is also utilized to crush the calculi. Matsumoto et al. (2005) [5] showed that using the ultrasound not only with high frequency for the individual bubbles in the bubble cloud but also with low frequency that agrees with the natural frequency of the cloud are effective in crushing the calculi. Also, the ultrasound has been used to increase the cell membrane permeability. The technique has been developed as a non-viral strategy for the intracellular delivery of the DNAs and anticancer drug [6,7]. The biophysical mechanism of the process using ultrasound is called “sonoporation.” The sonoporation is facilitated by the presence of microbubbles. However, due to the complexity of the interaction between the ultrasound, microbubbles, and cavitation bubbles generated by ultrasound, the mechanism has not been fully understood and the precise investigation is needed.

To investigate the mechanism of above phenomena, it is important to understand the collapse of interacting multiple bubbles. There are generally two theoretical approaches to the dynamics of a cluster of bubbles. One deals with the macroscopic motions of the bubble cluster by using the averaged equations of conservation of momentum and mass of liquid and gas [8-10]. In the analysis, the dynamics of bubble cloud is solved using the averaged equation for a bubbly liquid coupling with a set of equations for the single spherical bubble. The other is to analyze the microscopic motions of individual bubbles. Chahine and Liu (1985) [11] investigated collapse and growth of a bubble cluster using a singular perturbation method.

Fujikawa and Takahira (1986) [12] studied the effects of the interaction on the pressure waves radiated from two spherical gas bubbles in a compressible liquid. Chahine and Duraiswami (1992) [13] investigated the dynamics of the multiple bubbles by using the boundary integral method. Takahira et al. (1994) [14] studied the dynamics of a cluster of bubbles theoretically using the series expansion of the spherical harmonics. Although a lot of theoretical or numerical works were conducted for bubble-bubble interactions in the microscopic view point, most of works were restricted to the cases for the collapse of spherical bubbles or slightly non-spherical bubbles, and for the nonspherical bubble collapse in incompressible liquids.

In the present work, to understand the influence of microscopic motion of each bubble on the macroscopic motion of bubble cluster, we conduct direct numerical simulation for the collapse of interacting bubbles in compressible liquids using the improved ghost fluid method (GFM) [15, 16]. In the method, the Riemann solutions are utilized to diminish the numerical pressure oscillations near the gas-liquid interfaces. Although the analysis of the shock-bubble/bubble-bubble interactions near a material boundary is important to investigate the material damage due to bubble collapse, the present study is restricted to the shock-bubble/bubble-bubble interactions in an infinite liquid to obtain the fundamental knowledge for the collapse of interacting multiple bubbles. In the present paper, the collapse of in-line two or three bubbles induced by an incident shock wave is investigated to clarify the influence of size and configuration of bubbles on the collapse.

NUMERICAL METHOD

The governing equations for the present analysis are the axi-symmetric Euler equations for compressible flows:

$$\begin{pmatrix}\rho\\ \rho u\\ \rho v\\ E\end{pmatrix}_t+\begin{pmatrix}\rho u\\ \rho u^2+p\\ \rho uv\\ (E+p)u\end{pmatrix}_r+\begin{pmatrix}\rho v\\ \rho uv\\ \rho v^2+p\\ (E+p)v\end{pmatrix}_z=-\frac{1}{r}\begin{pmatrix}\rho u\\ \rho u^2\\ \rho uv\\ (E+p)u\end{pmatrix}, \qquad (1)$$

where t is time, r and z are the coordinates, ρ is the density, u and v are velocities in the r and z directions, respectively, E is the total energy per unit volume and p is the pressure. The subscripts t, r, and z indicate the differentiation with respect to t, r, and z, respectively. The third order TVD Runge-Kutta scheme and the third order ENO-LLF scheme [17] are used for time and space discretization of Euler equations, respectively.

We use the following stiffened equation of state for air and water:

$$p=(\gamma-1)\rho e-\gamma\Pi, \qquad (2)$$

where e is internal energy per unit mass, γ and Π are parameters for the characteristic of materials. The following γ and Π are utilized in the simulation:

Air: $\gamma=1.4,\ \Pi=0$ Pa,

Water: $\gamma=4.4,\ \Pi=6\times10^8$ Pa.

The level set function, φ, is utilized to determine interface location. φ is the signed distance function from the interface. The location of the interface is defined as a set of points where φ =0. We define that the region where φ <0 is for water (see Fig. 1). Thus the physical properties for water are utilized in the region where φ <0. The region where φ >0 is for air. After determining the region, φ is advanced in time by solving the following equation:

$$\frac{\partial\varphi}{\partial t}+u\frac{\partial\varphi}{\partial r}+v\frac{\partial\varphi}{\partial z}=0. \qquad (3)$$

To maintain φ as a true distance function, the following reinitialization equation is solved [18].

$$\frac{\partial\varphi}{\partial\tau}+S(\varphi_0)(1-|\nabla\varphi|)=0, \qquad (4)$$

where $S(\varphi_0)=\varphi_0/\sqrt{\varphi_0^2+h^2}$ is the sign function of $\varphi_0(=\varphi(\tau=0))$ with appropriate numerical smearing and h is the grid spacing. After solving Euler equations and Eq. (3), Eq. (4) is solved until it converges near the interface in fictitious time, τ. Using the level set function, the unit normal at each grid point is defined as $\boldsymbol{n}=\nabla\varphi/|\nabla\varphi|$. We use the third order TVD Runge-Kutta scheme and the fifth order WENO scheme [19] for time and space discretization of Eqs. (3) and (4), respectively. In the advancement of the level set function with Eq. (3), the level set function is corrected by using the hybrid particle level set method [20] to conserve mass. The hybrid particle level set method is effective in conserving the mass of the collapsing bubble.

The GFM is utilized in solving two kinds of fluids with different physical properties. In the method, ghost fluids are defined at every grid point in the computational domain so that each grid point contains the mass, momentum, and energy for real fluid that exists at that grid point, and a ghost mass, momentum and energy for the other fluid that does not really exist at that grid point [21]. In the present work, two kinds of ghost fluids are defined in the computational domain. Once the ghost fluids are defined, standard method for single-phase fluid can be utilized to update Euler equations. After updating Euler equations for each fluid separately, the level set function is utilized to decide which of the two fluids is valid at each grid point. The valid fluid is kept and the other is discarded so that only one fluid is defined at each grid point.

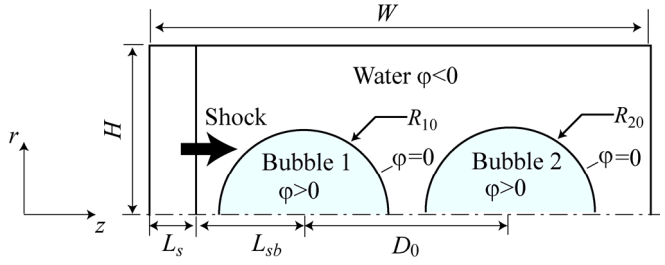

Figure 1: Schematic of numerical model.

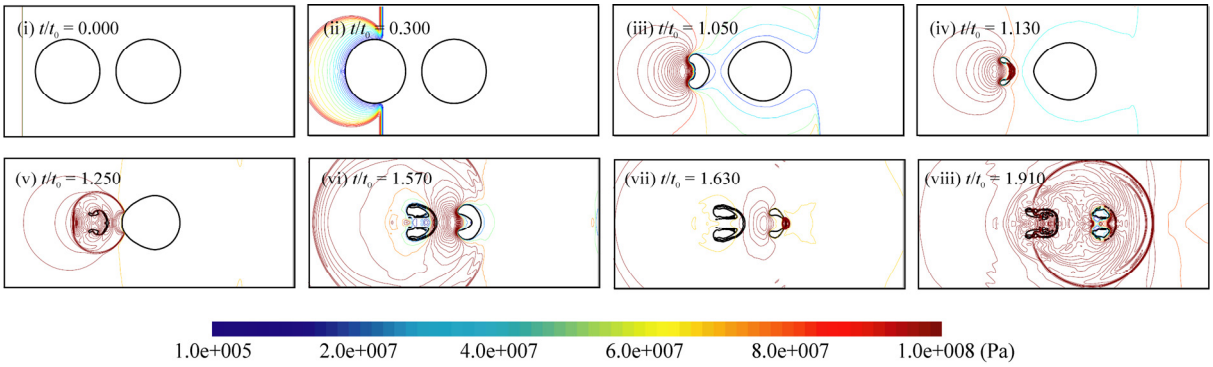

Figure 2: Pressure contours for the collapse of in-line two bubbles (D_0/R_{10}=2.5 and w=1.0).

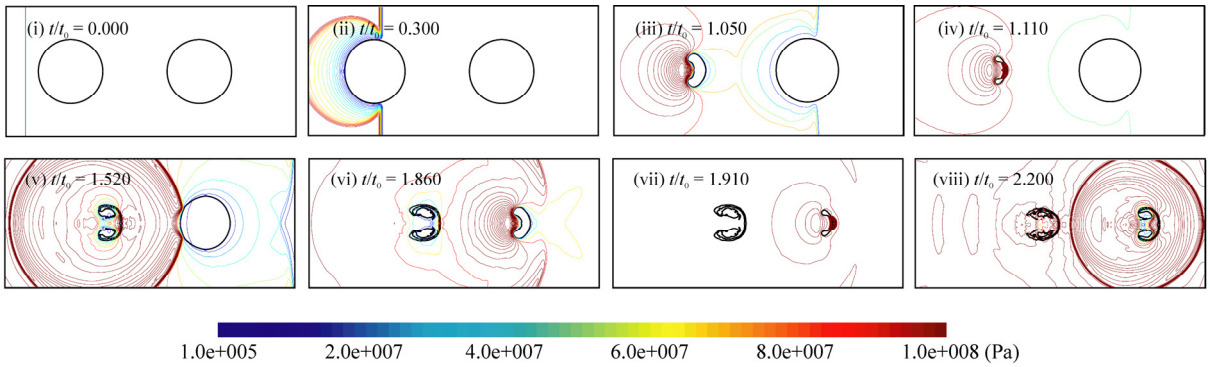

Figure 3: Pressure contours for the collapse of in-line two bubbles (D_0/R_{10}=4.0 and w=1.0).

In the application of the GFM, to avoid unrealistic pressure oscillations due to the large sensitivity of the gas-liquid interface [22], the values on both sides of the interface are corrected by using the values at the neighboring nodes and the values obtained from the solutions of the Riemann problem at the interface [15, 16]. We corrected the values on both sides of the interface by using the one-dimensional Riemann solutions in each direction of the coordinates with iterative algorithm [15, 16, 23]. In the improved GFM, the definition of ghost values is also modified as follows [15, 16]. For the ghost fluid of gas, the pressure as well as entropy and tangential velocity are extrapolated from real gas. For the ghost fluid of liquid, the normal velocity as well as entropy and tangential velocity are extrapolated from real liquid. We use the fast extension method based on the Fast Marching Method for the extrapolation [24]. In the Fast Marching Method, a physical variable I to be extrapolated is determined by using the following equation:

$$\nabla\varphi \cdot \nabla I = 0. \qquad (5)$$

The central difference is utilized to calculate spatial derivative in Eq. (5).

RESULTS

Interactions of Shock Waves with In-Line Two Bubbles

The computational domain and bubble arrangement are shown in Fig. 1. The initial radius of the upstream bubble (Bubble 1) is R_{10} and that of downstream bubble (Bubble 2) is R_{20}. R_{10} is taken to be 1.5 mm in the present analysis. The initial distance between the centroid of Bubble 1 and Bubble 2 is D_0. The bubbles are initially at rest. An incident shock wave propagates from the left-hand side of the bubbles. The initial distance between the shock front and the bubble centroid is L_{sb}. The initial computational region behind the incident shock is L_s. The height of the computational domain is H and the width of the domain is W. The typical values used in the present computation are L_{sb}= 2.1 mm, L_s=2.4 mm, H = 6 mm, and W = 18 mm. The domain is divided by a square mesh with $0.02R_0$. Symmetric boundary conditions are used at the centerline of the domain. Nonreflection boundary conditions are applied to the top, left and right boundaries. The pressure behind the incident plane shock wave is taken to be p_s=100 MPa. The pressure and density of pre-shocked water are taken to be p_0=101.3 kPa and 998.6 kg/m^3, respectively. The initial density and velocity of post-shocked water are determined from the Rankine-Hugoniot jump condition. The initial density of air is taken to be 1.26 kg/m^3. In the present analysis, the characteristic time of bubble collapse is evaluated with $t_0 = R_{10}/\sqrt{\Delta p/\rho_s}$ where Δp=p_s–p_0 and ρ_s is the initial density behind the shock wave. Thus increasing Δp decreases t_0. The other characteristic time is given by $t_D = D/a_s$ that is the time when the pressure waves pass through in-line bubbles where a_s ($=\sqrt{(p_s+\Pi)/\rho_s}$) is the speed of sound in a liquid. If $t_D/t_0 \ll 1$, the bubbles start to collapse under almost the uniform increase in pressure due to the propagation of the incident shock wave. However, if p_s is large, the arrival time of the incident shock wave at each bubble

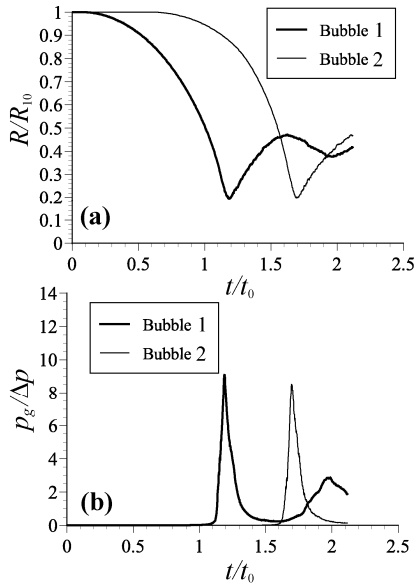

Figure 4: Time histories of bubble radii and average pressures inside the bubbles when D_0/R_{10}=2.5 and w=1.0.

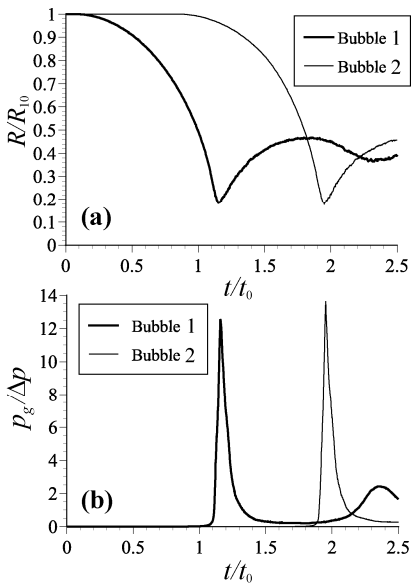

Figure 5: Time histories of bubble radii and average pressures inside the bubbles when D_0/R_{10}=4.0 and w=1.0.

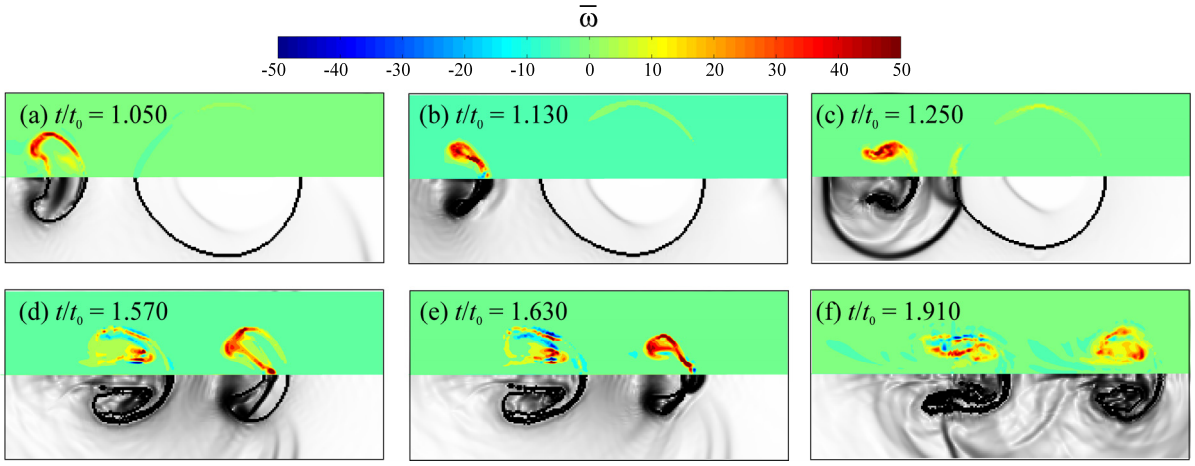

Figure 6: Vorticity distributions (top) and numerical Schlieren images (bottom) for the collapse of in-line two bubbles (D_0/R_{10}=2.5 and w=1.0).

affects the collapse of in-line bubbles. Thus the choice of p_s is important in the bubble-bubble/shock-bubble interactions. A large value of p_s=100 MPa is chosen in the simulations because the main concern in the present study is the violent bubble collapse induced by the strong shock wave as can been seen in the Extracorporeal Shock Wave Lithotripsy. The interactions of moderate or weak shock waves with bubbles will be simulated in the future works.

Figure 2 shows the pressure contours when the initial distance between the centers of two bubbles is D_0/R_{10}=2.5. Also, the pressure contours in the case of D_0/R_{10}=4.0 are shown in Fig. 3. For both cases, the ratio of initial bubble radii, w, is $w=R_{20}/R_{10}$=1.0. The time indicated in the figure is normalized by t_0.

When the incident shock impacts the bubble, an expansion wave is produced in water (Figs. 2(ii) and 3(ii)) because the acoustic impedance of air is smaller than that of water. When the incident shock wave interacts with Bubble 1, the deformation occurs on the bubble surface immediately after the shock impacts the bubble. The upstream surface is depressed and the liquid jet is formed on this side (Figs. 2 (iii) and 3(iii)). When the distance D_0/R_{10} is short, the interface of the upstream side of Bubble 2 is elongated toward Bubble 1 because of the sink flow induced by the collapse of Bubble 1 (see (iii) and (iv) in Figs. 2 and 3). When the jet impacts the downstream surface, the shock wave due to the impact of liquid jet (SWJ) is formed at the point of jet-impact (Figs. 2(iv) and 3(iv)). When the bubble rebounds, the rebounding shock wave (RSW) is

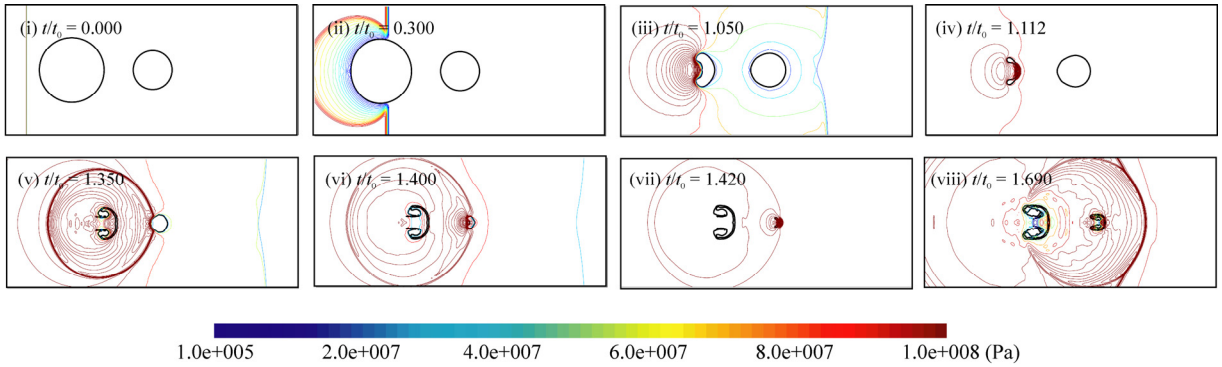

Figure 7: Pressure contours for the collapse of in-line two bubbles (D_0/R_{10}=2.5 and w=0.6).

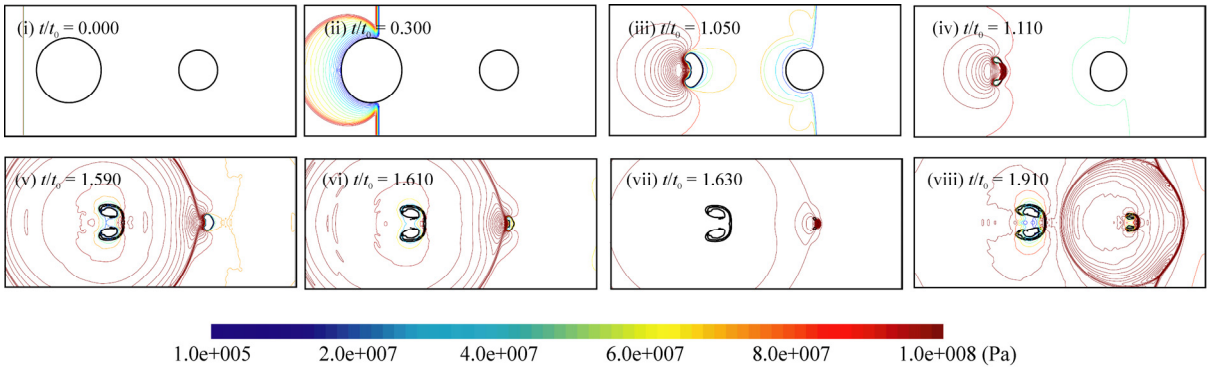

Figure 8: Pressure contours for the collapse of in-line two bubbles (D_0/R_{10}=4.0 and w=0.6).

generated from the toroidal bubble. The SWJ and RSW impact Bubble 2 (Figs. 2(v) and 3(v)), which leads to the formation of a liquid jet on the upstream surface of Bubble 2 (Figs. 2(vi) and 3(vi)). The jet impacts the downstream surface of Bubble 2 and the SWJ is generated at the point of jet-impact (Figs. 2(vii) and 3(vii)). After that, the RSW is formed from Bubble 2. Both the SWJ and RSW propagate in the water (Figs. 2(viii) and 3 (viii)).

Figure 4 shows the time histories of (a) bubble radii and (b) average gas pressures inside the bubbles p_g when D_0/R_{10}=2.5. The thick and thin solid lines denote Bubble 1 and 2, respectively. The time histories for D_0/R_{10}=4.0 are shown in Fig. 5. As the bubble volume becomes small, the internal gas pressure becomes high. In Fig. 4 (b), the maximum gas pressure of Bubble 2 is lower than that of Bubble 1. On the other hand, the maximum pressure of Bubble 2 is slightly higher than that of Bubble 1 in Fig. 5(b). Thus, whether the collapse of Bubble 2 is accelerated or not is dependent on the bubble-bubble distance. Since the expansion wave is reflected on the surface of the Bubble 2 after the incident shock wave hits the Bubble 2, Bubble 1 collapses under the lower pressure field than that without Bubble 2. Therefore, decreasing the bubble-bubble distance decelerates the collapse of Bubble 1; the collapse period in Fig. 4 is longer than that in Fig. 5; the maximum internal gas pressure of Bubble 1 in Fig. 4(b) is lower than that in Fig. 5(b); the shock waves generated from Bubble 1 is weaker in Fig. 4. Thus, the collapse of Bubble 2 is not accelerated in D_0/R_{10}=2.5.

The vorticity distributions (top) and numerical Schlieren images (bottom) are shown in Fig. 6 for the case of D_0/R_{10}=2.5. The nondimentionalized vorticity $\bar{\boldsymbol{w}} = \boldsymbol{w} \times t_0$ is plotted in the figure. The positive and negative vorticities denote the counterclockwise and clockwise rotations, respectively. In the shock-bubble interactions, the vorticity is produced due to the misalignment of gradients in pressure and density by the following vorticity equation.

$$\frac{\mathrm{d}\boldsymbol{w}}{\mathrm{d}t} = (\boldsymbol{w}\cdot\nabla)\boldsymbol{u} - \boldsymbol{w}\nabla\cdot\boldsymbol{u} + \frac{\nabla\rho\times\nabla p}{\rho^2}. \qquad (6)$$

After the incident shock wave passes through the bubble, the counterclockwise vorticity is generated for Bubble 1. The magnitude of the vorticity becomes large as the liquid jet develops (Fig. 6(a)). When the liquid jet impacts the downstream surface of Bubble 1, the high vorticity region spreads around the whole surface (Fig. 6(b)). After the jet impacts, the bubble becomes a toroidal shape and the circulation flow is induced around the bubble; the counterclockwise vorticity is observed around the thin gas layer ahead of the toroidal bubble (Fig. 6(c)). After the bubble rebounds, the clockwise vorticity is also produced around the bubble surface (Fig. 6(d)). For Bubble 2, in the same manner as Bubble1, the counterclockwise vorticity is generated, and becomes higher as the liquid jet develops (see Figs. 6(d), (e) and (f)). In the case of D_0/R_{10}=2.5, the magnitude of the counterclockwise vorticity is larger for the downstream bubble

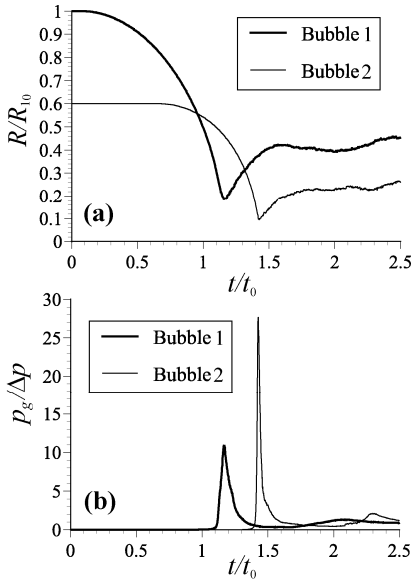

Figure 9: Time histories of bubble radii and average pressures inside the bubbles when D_0/R_{10}=2.5 and w=0.6.

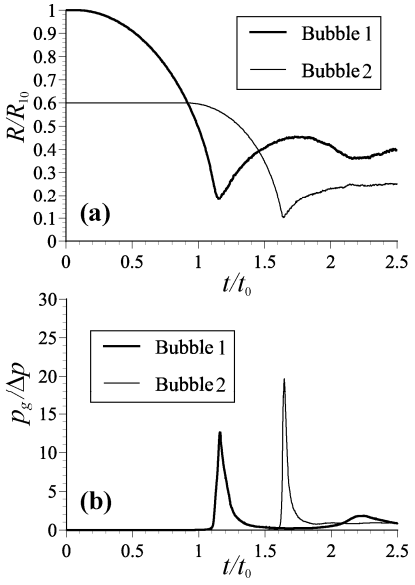

Figure 10: Time histories of bubble radii and average pressures inside the bubbles when D_0/R_{10}=4.0 and w=0.6.

than that for the upstream bubble. This may be due to the impact of the shock waves generated from the upstream bubble on the downstream bubble. Although the vortex structure around bubbles is very important in the shock-bubble interactions and a lot of studies have been done for the production of the baroclinic vorticity [25, 26], we will not discuss on this hereinafter, because the increase in pressure due to the bubble-bubble/shock-bubble interactions is main concern in the present study. The detailed mechanism of the formation of the baroclinic vorticity will be discussed in the future works.

Figures 7 and 8 show the pressure contours when $w=R_{20}/R_{10}$=0.6. The initial distance is taken to be D_0/R_{10}=2.5 in Fig. 7 and D_0/R_{10}=4.0 in Fig. 8. Figure 9 shows the time histories of bubble radii and average pressures inside the bubbles p_g for D_0/R_{10}=2.5. The time histories for D_0/R_{10}=4.0 are shown in Fig. 10. Although the expansion wave caused by the reflection of the incident shock wave on the surface of Bubble 2 decelerates the collapse of Bubble 1, the influence of Bubble 2 is weak in the case of w= 0.6 because the Bubble 2 is smaller than Bubble 1. However, the collapse of Bubble 1 affects Bubble 2 more strongly when the downstream bubble is smaller than the upstream bubble; the maximum pressure of Bubble 2 is much higher than that of Bubble 1 in both Figs. 9(b) and 10(b).

Figures 11 and 12 show the relationship between the initial distance between two bubbles D_0/R_{10} and the maximum average pressure inside the bubble $p_g^{\max}$ when w=1.0 and w=0.6, respectively. The maximum pressure is normalized by p_c where p_c is the maximum average gas pressure when the single bubble collapses by the same incident shock wave as that for the collapse of in-line two bubbles shown above. Thus, as D_0/R_{10} tends to infinity, $p_g^{\max}/p_s$ tends to 1. The open triangle denotes the maximum pressure of Bubble 1 and the closed circle denotes that of Bubble 2. When w=1.0 in Fig. 11, $p_g^{\max}$ for Bubble 1 decreases monotonically with the decrease of D_0. This is due to the influence of expansion wave caused by the

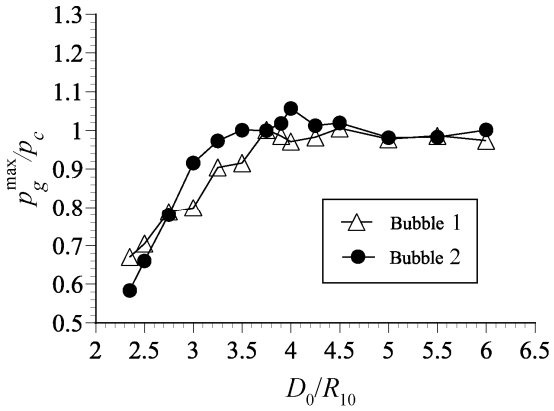

Figure 11: The relationship between the initial distance between two bubbles and the maximum average pressure inside the bubbles (w=1.0).

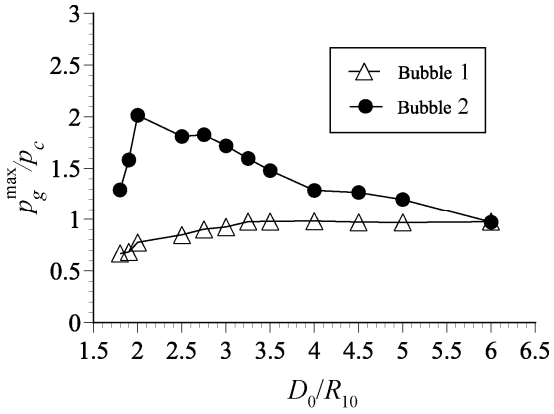

Figure 12: The relationship between the initial distance between two bubbles and the maximum average pressure inside the bubbles (w=0.6).

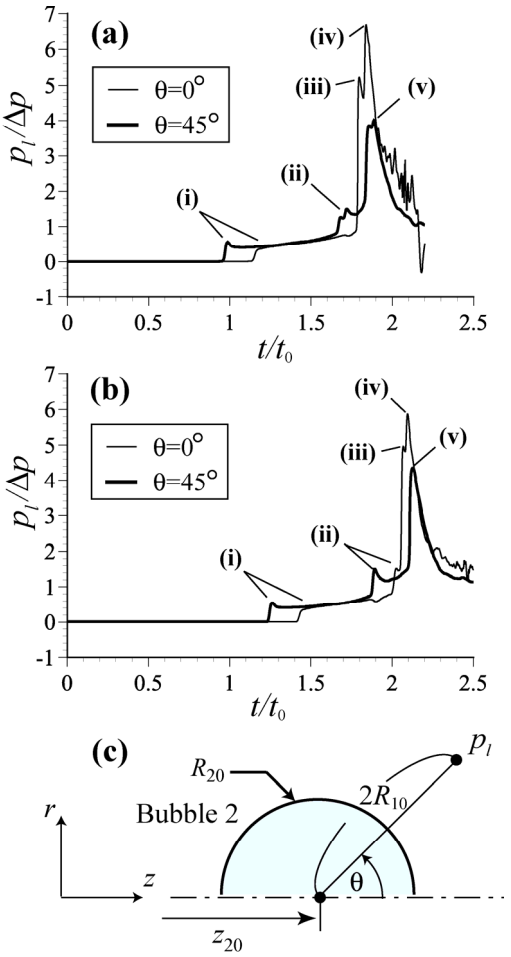

Figure 13: Time histories of (a) water pressure in the case of w=1.0 at θ=0 and 45 degrees for D_0/R_{10}=2.5 and

reflection of the incident shock wave on the downstream bubble. The gentle maxima is seen at about D_0/R_{10}=4.0 in $p_g^{\max}$ for Bubble 2 although the limiting tendency for $D_0/R_{10} \to 1$ and $D_0/R_{10} \to \infty$ is the same as Bubble 1. On the other hand, when w=0.6, the local maxima is seen clearly at about D_0/R_{10}=2.0 in $p_g^{\max}$ for Bubble 2. Also, $p_g^{\max}$ for Bubble 2 is always higher than p_c for the single bubble. These results suggest that the collapse of the downstream smaller bubble than the upstream bubble can collapse violently owing to the interaction with the shock waves generated from the upstream bubble. Also, there exist the bubble-bubble distance in which the collapse of the downstream bubble is most accelerated. This condition depends on the phase of the downstream bubble at the impact of the shock waves generated from the upstream bubbles. Fujikawa and Takahira (1986) [12] showed that there exited a bubble-bubble distance where the collapse of the initially smaller bubble was accelerated by the collapse of the initially larger bubble when two spherical bubbles collapsed in an infinite space. In their analysis, since the stepwise pressure increase was applied simultaneously around the bubbles, the acceleration of the initially smaller bubble was not achieved at the first collapsing stage. However, since the propagation of the

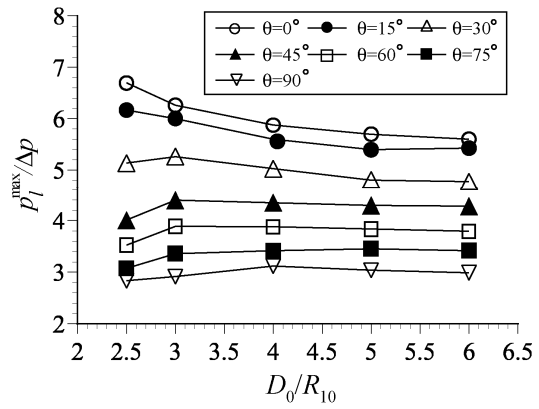

Figure 14: The maximum water pressure around Bubble 2 versus the initial distance between two bubbles when w=1.0.

incident shock wave causes the collapse of a bubble in the present situation, the collapsing phase of each bubble is not the same even though two bubbles with the initially same radii collapse. The difference of the collapsing phase of each bubble causes the acceleration of the downstream bubble.

Figure 13 shows the time histories of water pressure p_l at several points around Bubble 2 when w=1.0. The schematic of measuring points is shown in Fig. 13(c). The location of the measuring points is given by $z = z_{20} + 2R_{10}\cos\theta$ and $r = 2R_{10}\sin\theta$ where z_{20} is the initial location of the center of Bubble 2 in the z direction. The time histories at the points of θ=0 degree (thin line) and 45 degree (thick line) are shown in Figs. 13 (a) and (b) which are corresponding to D_0/R_{10}=2.5 and D_0/R_{10}=4.0, respectively. When the incident shock wave reaches the measuring point, the sudden pressure increase, which is indicated by (i) in each figure, is observed. Then, the pressure increase due to the propagation of two kinds of shock waves (SWJ and RSW) generated from the Bubble 1 is observed (see (ii) in Fig. 13). Since the shock waves are reflected by the Bubble 2, this pressure increase is not clearly seen at θ=0 degree. After the liquid jet impacts the downstream surface of Bubble 2, the steep pressure peak due to the SWJ is seen in (iii) of Fig. 13. Immediately after the arrival of the SWJ from Bubble 2, the RSW arrives at the measuring point at θ=0 degree (see (iv)). The RSW from the Bubble 2 results in the maximum pressure at the point. After that, both the SWJ and RSW from Bubble 2 pass through the point of θ=45 degree (v), which results in the steep increase of liquid pressure. It should be noted that although the maximum internal gas pressure of Bubble 2 is higher in the case of D_0/R_{10}=4.0 than that in the case of D_0/R_{10}=2.5 (see Fig. 11), the liquid pressure at the point of θ=0 degree is higher in the case of D_0/R_{10}=2.5. This is because the pressure increase in water due to the upstream bubble is higher when the bubble-bubble distance is short.

To understand the influence of bubble-bubble distance on the pressure increase in water shown in Fig. 13, the maximum water pressure $p_l^{\max}$ around Bubble 2 is plotted versus the initial bubble-bubble distance D_0/R_{10} in Fig. 14. In the figure, w

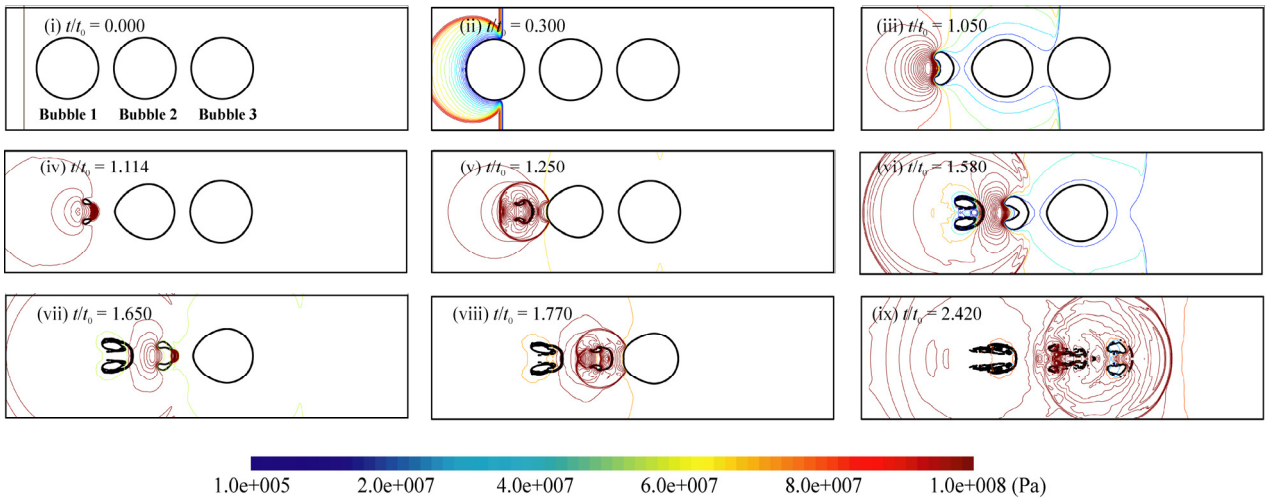

Figure 15: Pressure contours for the collapse of in-line three bubbles (D_0/R_{10}=2.5 and w=1.0).

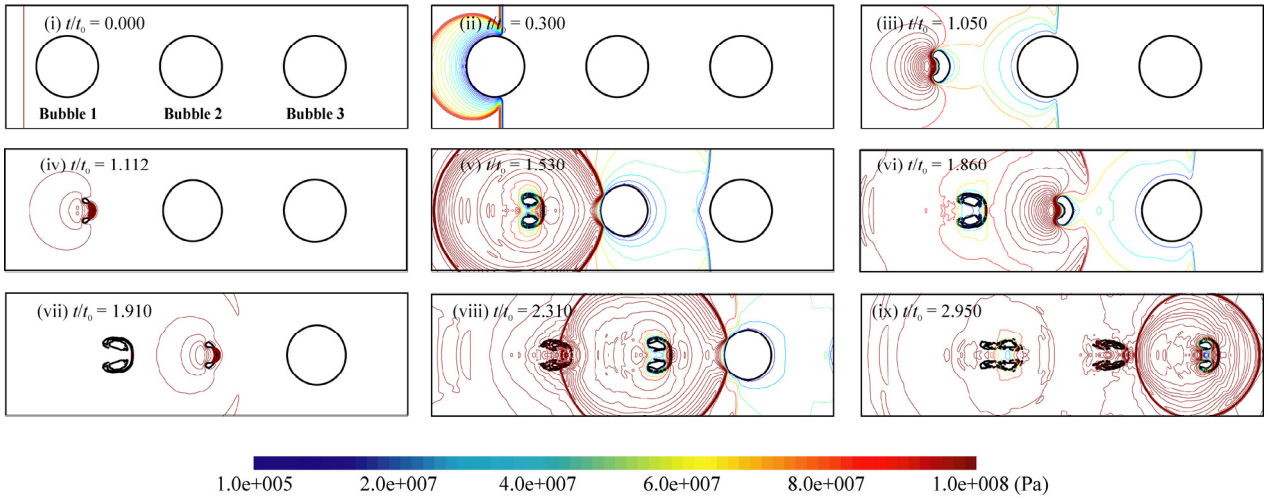

Figure 16: Pressure contours for the collapse of in-line three bubbles (D_0/R_{10}=4.0 and w=1.0).

(the ratio of Bubble 1 and 2) is 1.0 and the measuring points in Fig. 13 (c) are taken to be θ=0, 15, 30, 45, 60, 75, and 90 degrees. It is found that the closer the measuring point is to the axis of symmetry, the higher the liquid pressure is for any D_0/R_{10}. The pressures at θ=0 and 15 degrees decrease monotonically with the increase of the bubble-bubble distance. On the other hand, the maximum liquid pressure takes the gentle local maxima for large θ. These results show that the maximum pressure increase can be high with the decrease of the bubble-bubble distance although the pressure increase in liquid depends on the measuring points.

Interactions of Shock Waves with In-Line Three Bubbles

Figures 15 and 16 show the pressure contours of the collapse of three bubbles with the same initial radii (w=R_{20}/R_{10}=R_{30}/R_{10} =1.0, where R_{30} is the radius of Bubble 3). The most downstream bubble is called Bubble 3. In the following results, the initial distance between Bubbles 1 and 2 is always the same as that between Bubbles 2 and 3. Thus, we use the same expression of D_0 for the initial distance between the bubbles as used in the in-line two bubbles (see Fig. 1). Figures 14 and 15 correspond to the results when D_0/R_{10}=2.5 and 4.0, respectively. In the simulation for the collapse of three bubbles, the width of computational domain is taken to be W=24 mm. Figure 17 shows the time histories of bubble radii and average pressures inside the bubbles p_g for D_0/R_{10}=2.5. The time histories for D_0/R_{10}=4.0 are shown in Fig. 18.

Since the first collapsing stage of Bubble 1 ends before the expansion wave caused by the reflection of the incident shock wave on the interface of Bubble 3 arrives at Bubble 1, the collapsing behavior of Bubble 1 is not affected by the Bubble 3. When the distance between the Bubbles 2 and 3 is sufficiently large as in Fig. 16, the collapsing behavior of Bubble 2 is not also affected by the Bubble 3. Therefore, the collapsing behaviors of Bubbles 1 and 2 are very similar to those shown in Figs. 2 and 3 for in-line two bubbles. When D_0/R_{10}=2.5, the collapse of Bubble 2 is slightly affected by Bubble 3 because of the expansion wave caused by the reflection on the interface of

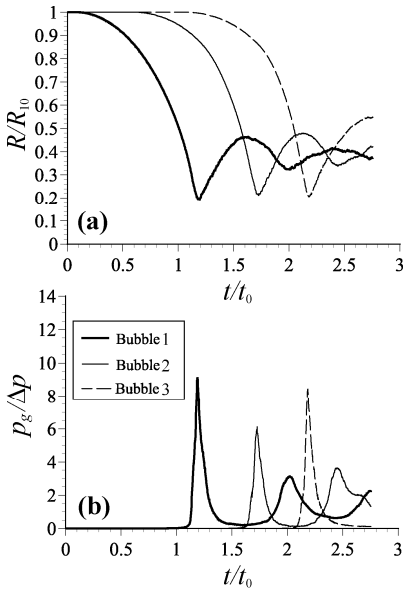

Figure 17: Time histories of bubble radii and average pressures inside the bubbles when D_0/R_{10}=2.5 and w=1.0.

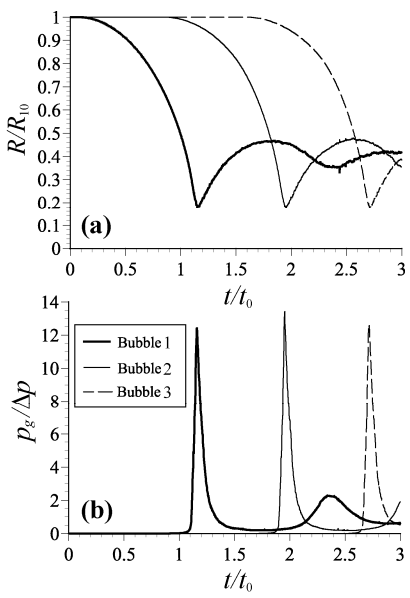

Figure 18: Time histories of bubble radii and average pressures inside the bubbles when D_0/R_{10}=4.0 and w=1.0.

Bubble 3; the maximum internal gas pressure of Bubble 2 for in-line three bubbles is lower than that for in-line two bubbles. On the other hand, the collapsing motion of Bubble 3 is affected by both Bubbles 1 and 2. When D_0/R_{10}=2.5, the maximum internal gas pressure becomes higher than that of Bubble 2 due to the shock waves generated from the Bubble 2. However, the maximum internal gas pressure of Bubble 3 is lower than that of Bubble 1 because the shock waves generated from the Bubble 2 is not so strong. Although Bubble 2 for D_0/R_{10} =4.0 collapses more violently than that for D_0/R_{10} =2.5, the collapse of Bubble 3 is not so accelerated because the distance between the bubbles is long. Consequently, the maximum internal pressure of Bubble 3 is almost the same as that of Bubble 1.

Figures 19 (a) and (b) show the time histories of water pressure around Bubble 3 when D_0/R_{10}=2.5 and 4.0, respectively. The measuring points of the pressure in water are the same as Fig. 13; the pressures at the points of θ=0 degree (thin line) and 45 degree (thick line) are shown in Fig. 19. As has been noted in Fig. 13 for in-line two bubbles, the sudden pressure increases due to the incident shock wave (i), the SWJ and RSW from Bubble 1 (ii), and the SWJ and RSW from Bubble 2 (iii) are seen in the pressure histories for in-line three bubbles. The steep pressure peaks indicated by (iv), (v), and (vi) are generated by the SWJ and RSW from Bubble 3. The comparison between Fig. 13 with Fig. 19 shows that the maximum liquid pressure for in-line three bubbles is higher than that for in-line two bubbles.

Figures 20 and 21 show the comparison of the maximum pressures in water around the downstream bubble between three cases of the single bubble, in-line two bubble, and in-line

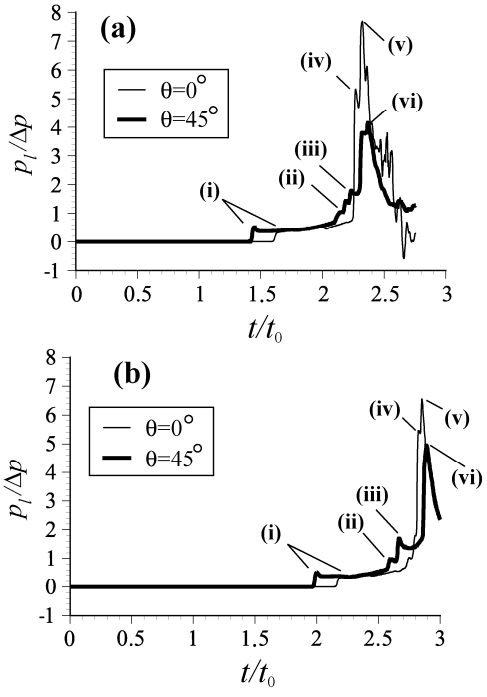

Figure 19: Time histories of water pressure around Bubble 3 when w=1.0: (a) D_0/R_{10}=2.5; (b) D_0/R_{10}=4.0.

three bubbles at various measuring points. The results for D_0/R_{10}=2.5 and 4.0 are shown in Figs. 20 and 21, respectively. In all measuring points, the maximum pressure for in-line three bubbles is higher than that for in-line two bubbles; in particular,

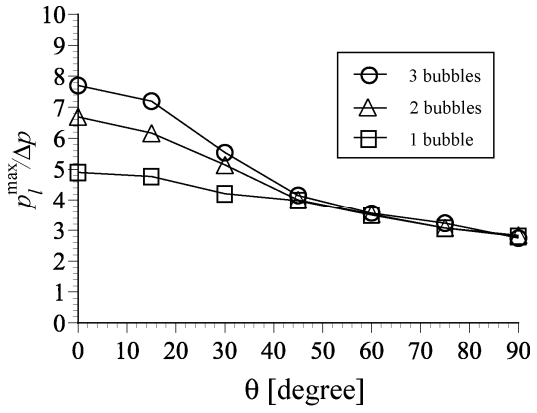

Figure 20: The maximum pressures in water at various points around the downstream bubble for the collapse of a single bubble (1 bubble), in-line two bubbles (2 bubbles), and in-line three bubbles (3 bubbles) (D_0/R_{10}=2.5 and w=1.0).

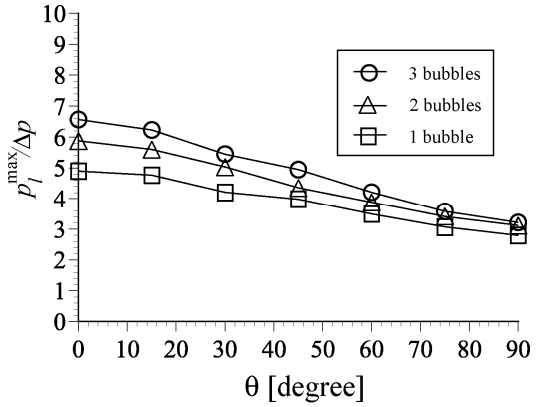

Figure 21: The maximum pressures in water at various points around the downstream bubble for the collapse of a single bubble (1 bubble), in-line two bubbles (2 bubbles), and in-line three bubbles (3 bubbles) (D_0/R_{10}=4.0 and w=1.0).

the pressure on the axis of symmetry is prominent. Also, the maximum pressure near the axis becomes higher with the decrease of the distance between the bubbles. This may be because that the pressure increase is induced by the superposition of pressure increase generated by the shock waves from all bubbles. These results indicate that the higher liquid pressure can be achieved near the axis of symmetry with the increase of number of bubbles and with the decrease of the distance between the bubbles.

CONCLUSION

In the present study, direct numerical simulations were conducted for the shock-bubble and bubble-bubble interactions by using the improved ghost fluid method in which the Riemann solutions were utilized to diminish numerical oscillations near interfaces. The collapse of in-line two bubbles and in-line three bubbles were simulated to clarify the conditions under which the bubble-bubble interactions accelerate or decelerate the bubble collapse. The influence of bubble size and bubble-bubble distance on the bubble collapse was discussed. It was shown that when the in-line bubbles collapse owing to the interaction with the incident shock wave, the collapse of the downstream bubble can be accelerated by the shock waves induced by the collapse of upstream bubbles. On the other hand, the collapse of the upstream bubbles was decelerated by the expansion wave cased by the reflection of the incident shock wave at the surface of the downstream bubbles. Also, it was found that there exists the bubble-bubble distance in which the collapse of the downstream bubble is most accelerated. It was also found that when the downstream bubble is smaller than the upstream bubble, the downstream bubble collapses more violently than the single bubble at any distance between the bubbles. The phase of the downstream bubble at the impact of the shock waves generated from the upstream bubbles is important in determining the acceleration of the collapse of the downstream bubble. The acceleration of the collapse of the downstream bubble is dependent on the phase of the collapse of the downstream bubble when the shock waves generated from the upstream bubbles impact the downstream bubble. The pressure increase in liquid around the downstream bubble was also discussed. The results showed that the liquid pressure increases near the axis of symmetry with the increase of number of bubbles and with the decrease of the bubble-bubble distance because the pressure increase in liquid is caused by the superposition of the shock waves generated from all bubbles.

REFERENCES

[1] Brennen, C. E. 1995, *Cavitation and bubble dynamics*, Oxford University Press, New York, USA.

[2] Bucheeri, A. et al. 2008, "Microbubble formation at a nozzle in liquid mercury," *J. Nuclear Sci. Tech.*, 45, 525-531.

[3] Futakawa, M. et al. 2008, "Mitigation technologies for damage induced by pressure waves in high-power mercury spallation neutron sources (II) -bubbling effect to reduce pressure wave-," *J. Nuclear Sci. Tech.*, 45, 1041-1048.

[4] Kodama, T. and Takayama, K. 1998, "Dynamic behavior of bubbles during extracorporeal shock-wave lithotripsy", *Ultrasound Med. & Biol.*, 24, 723-738.

[5] Matsumoto, Y. et al. 2005, "Medical ultrasound with microbubbles," *Exp. Therm. Fluid Sci.*, 29, 255-265.

[6] Hallow, D. M. et al. 2006, "Measurement and correlation of acoustic cavitation with cellular bioeffects," *Ultrasound Med. & Biol.*, 32, 1111-1122.

[7] Zhou, Y. et al. 2008, "Dynamics of sonoporation correlated with acoustic cavitation activities," *Biophys. J.*, 94, L51-L53.

[8] d'Agostino, L. and Brennen, C. E., 1989, "Linearized dynamics of spherical bubble clouds," *J. Fluid. Mech.*, 199, 155-176.

[9] Omta, R. 1987, "Oscillation of a cloud of bubbles of small and not small amplitude," *J. Acoust. Soc. Am.*, 82, 1018-1033.

[10] Matsumoto, Y. and Yoshizawa, S. 2005, "Behavior of a bubble cluster in an ultrasound field," *Int. J. Numer. Meth. Fluids*, 47, 591-601.

[11] Chahine, G. L. and Liu, H. L. 1985, "A singular-perturbation theory of the growth of a bubble cluster in a superheated liquid," *J. Fluid Mech.*, 156, 257-279.
[12] Fujikawa, S. and Takahira, H. 1986, "A theoretical-study on the interaction between 2 spherical bubbles and radiated pressure waves in a liquid," *Acustica*, 61, 188-199.
[13] Chahine, G. L. and Duraiswami, R. 1992, "Dynamic interactions in a multibubble cloud," *Trans. ASME, J. Fluid Eng.*, 114, 680-686.
[14] Takahira, H. et al. 1994, "Dynamics of a cluster of bubbles in a liquid (theoretical-analysis)," *JSME Int. J. Series B*, 37, 297-305.
[15] Takahira, H., Matsuno, T. and Shuto, K. 2008, "Numerical investigations of shock-bubble interactions in mercury," *Fluid Dyn. Res.,* 40, 510-520.
[16] Takahira, H., Kobayashi K. and Matsuno, T. 2009, "Direct numerical simulations of interaction of strong shock waves with nonspherical gas bubbles near glass boundaries in mercury," *Int. J. Emerging Multidisciplinary Fluid Sci.*, 1, 85-99.
[17] Shu, C.-W. and Osher, S. 1989, "Efficient implementation of essentially non-oscillatory shock capturing schemes II," *J. Compt. Phys*., 83, 32-78.
[18] Sussman, M., Smereka, P. and Osher, S. 1994, "A level set approach for computing solutions to incompressible two-phase flow," *J. Compt. Phys.*, 114, 146-159.
[19] Jiang, G.-S. and Peng, D. 2000, "Weighted ENO schemes for Hamilton-Jacobi equation," *SIAM J. Sci. Compt.*, 21, 2126-2143.
[20] Enright, D. et al. 2002, "A hybrid particle level set method for improved interface capturing," *J. Comput. Phys.*, 183, 83-116.
[21] Fedkiw, R. et al. 1999, "A non-oscillatory Eulerian approach to interfaces in multimaterial flows (the ghost fluid method)," *J. Comput. Phys.*, 152, 457-492.
[22] Fedkiw, R. 2002, "Coupling an Eulerian fluid calculation to a Lagrangian solid calculation with the ghost fluid method," *J. Comput. Phys.*, 175, 200-224.
[23] Nourgaliev, R., Dinh, N. and Theofanous, T. 2004, "Direct numerical simulation of compressible multiphase flows: interaction of shock waves with dispersed multimaterial media," *Proc. of the 5th Int. Conf. on Multiphase Flow*, Paper No. 494, 18 pages.
[24] Adalsteinsson, D. and Sethian, J. A. 1999, "The fast construction of extension velocities in level set methods," *J. Comput. Phys.*, 148, 2-22.
[25] Haas, J.-F. and Sturtevant, B. 1987, "Interaction of weak shock waves with cylindrical and spherical gas inhomogeneities," *J. Fulid Mech.*, 181, 41-76.
[26] Niederhaus, John H. J. et al. 2008, "A computational parameter study for the three-dimensional shock–bubble interaction," *J. Fulid Mech.*, 594, 85-124.